Author/s:
Ng, C;Wesemann, L;Panchenko, E;Song, J;Davis, TJ;Roberts, A;Gomez, DE

Title:
Plasmonic Near-Complete Optical Absorption and Its Applications

Date:
2019-07-01

Citation:
Ng, C., Wesemann, L., Panchenko, E., Song, J., Davis, T. J., Roberts, A. & Gomez, D. E. (2019). Plasmonic Near-Complete Optical Absorption and Its Applications. ADVANCED OPTICAL MATERIALS, 7 (14), https://doi.org/10.1002/adom.201801660.

Accepted for publication in *Advanced Optical Materials*

PROGRESS REPORT

Plasmonic near-complete optical absorption and its applications

Charlene Ng[1] | Lukas Wesemann[2] | Evgeniy Panchenko[2] | Jingchao Song[2] | Timothy J. Davis[2] | Ann Roberts[2] | Daniel E. Gómez[3]

[1]Leibniz-Institut für Polymerforschung Dresden e.V., Institute of Physical Chemistry and Polymer Physics, 01069 Dresden, Germany

[2]School of Physics, The University of Melbourne, 3010, Australia

[3]School of Science, RMIT University, Melbourne, VIC, 3000, Australia

Correspondence
School of Physics, The University of Melbourne, 3010, Australia
Email: ann.roberts@unimelb.edu.au

Near-complete absorption of light has the potential to underpin advances in photodetection, advanced chemistry, coloration of materials and energy. Here we report recent progress on the development of metasurfaces and thin film structures that produce strong absorption bands in the visible and longer wavelength regions of the electromagnetic spectrum, due in part to the excitation of plasmonic resonances. We discuss proof-of-concept demonstrations and applications of these in chemical sensing, the generation of structural colour, the creation of optoelectronic devices and photocatalysis. Future applications are also discussed.

KEYWORDS
Metamaterials, absorbers, plasmonics, hot carriers, nanofabrication

1 | INTRODUCTION

Light absorption is of fundamental significance to photosynthesis, arguably one of the most important chemical reactions on this planet, but light absorption is also of key importance in many technological applications including optical sensors and photovoltaics. In photovoltaics, poor charge mobilities limit power-conversion efficiencies and consequently, it is highly desirable to use active layers that are both (ultra) thin but highly absorptive. We here report on recent progress in the use of nanostructured and uniform metallic (plasmonic) thin films that exhibit strong absorption in particular wavelength bands. We focus on relatively narrowband absorption, although an excellent overview of related approaches to broadband absorption has been published recently [1].

Fundamentally, the maximum amount of light that a infinitesimally thin layer of a material can absorb is 50% [2, 3], posing a limit to energy conversion efficiencies with devices utilizing absorption of light. It is, however, possible to engineer artificial materials that are extremely thin and can absorb nearly 100% of the incident light. The most common approach to achieving *near perfect absorption* (NPA) of light consists of "blocking" the possibility of transmission by, for example, using a reflective surface. Under these circumstances, the amount of light absorbed is controlled by the reflectance of the material, since, in these cases, the absorption is given by $A = 1 - |r|^2$. Clearly, high absorption can be obtained when there is vanishing reflectance ($r = 0$), which takes place under conditions of optical impedance matching [4]. In the following section, we discuss physical interpretations and mechanisms that have been employed for achieving near complete absorption of light using metallic nanostructures, including metasurfaces, as the absorptive element. This is followed by an overview of the applications of near-perfect absorption in fields such as chemical sensing, opto–electronics and photocatalysis. This review ends with an outlook. We note that near-perfect absorption can be achieved with a wide range of materials, for which excellent review papers have been previously published [5, 6, 7]

2 | THE PHYSICS OF PERFECT ABSORPTION

2.1 | Thin film perfect absorbers: Interference

As an introduction, we first review simple thin film approaches to NPA since these play a fundamental role in understanding the underlying physics. Optical thin-film coatings are essential in optical systems today and the simplest example of a thin-film absorber consists of a stack of an optically thin metal film, a thin dielectric film and a highly-reflective metallic film. Thin film coatings are widely used as anti- and high-reflection coatings, beamsplitters and wavelength filters on lenses, windows, displays [8] and absorbers for efficiency enhancements in photovoltaic cells [9], as well light emitting diodes (LED) and photodetectors [10]. Their characteristics, design and fabrication have been studied for over a century and are well-known [4]. In the next section, we will further discuss thin film absorbers where one layer is textured on the nanoscale, but thin-film systems are particularly useful as optical absorbers exhibiting distinct advantages over nano-structured optical metasurfaces. While textured surfaces require an additional level of processing, potentially requiring complex, top-down nanofabrication techniques [11, 12, 13], uniform thin-film structures are most commonly fabricated by electron beam or thermal evaporation, ion-beam or plasma sputtering, or other vapor deposition techniques, thus enabling comparably low-cost, large-area device fabrication [4].

Thin-film perfect absorbers are designed such that destructive interference effects associated with light reflected from the different layers within the structure minimize reflection and enhance absorption in metallic layers. Such thin-film NPA based on Fabry-Pérot type cavities has recently gained attention and dates back to the invention of the Salisbury screen [16]. The Salisbury screen (Figure 1) consists of a thin, transparent dielectric layer sandwiched between a semi-transparent thin metallic film and a fully reflective metallic substrate [17, 18, 19, 6]. This simple metal-insulator-metal (MIM) structure can achieve angle-of-incidence-dependent NPA over a narrow range of wavelengths. Experimentally, simple Ag/SiO_2/Ag stacks have been shown to result in large-area narrow bandwidth (17 nm) absorbances of up to 97%, at wavelengths that can be controlled to take place across the optical region of the electromagnetic spectrum [15, 6]. MIM absorbers incorporating other metals such as Au, Cu, Al and Ni have also been studied [18]. The findings suggest that structures utilizing, Au, Ag and Cu, in particular, yield distinct resonances in the optical range. Instead of relying on metallic mirrors, dielectric Bragg-reflectors (DBR) have been demonstrated as alternative back reflectors in Salisbury type thin-film absorbers with comparable absorption efficiencies [20]. Research into MIM absorbers based on highly doped silicon layers could further demonstrate the extension of the principle towards near- and mid-infrared wavelengths [21]. By doping silicon, characteristics of noble metals usually observed at

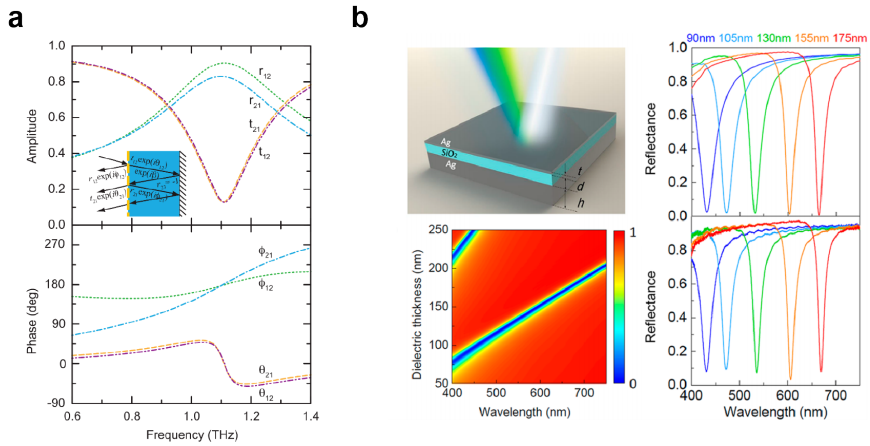

FIGURE 1 Near-perfect absorption in optical thin-film structures. a) Interference as the mechanism for near perfect absorption in MIM structures (c.f. inset). Shown are the amplitude and phase of the reflection and transmission coefficients at the air spacer interface with cross shaped metal resonators [14]. b) Optical Fabry-Pérot type thin film absorber based on MIM configuration. Shown is the schematic configuration and the simulated and measured reflectance spectrum of a Ag-SiO_2-Ag device [15]

visible frequencies, such as high cavity mode confinement and low loss, become available in the infrared spectral region.

One way to physically explain the phenomenon of perfect absorption in this MIM structure relies on textbook interference theory [22]. According to this interpretation, NPA occurs due to destructive interference between direct reflection at the air-absorber interface, and the subsequent multiple reflections taking place between the absorber-mirror interfaces for a spacing of approximately a quarter-wave between the reflective surfaces. The total phase accumulation must be an integer multiple of 2π, which can be written down in terms of the different contributions as: $m2\pi = \phi_I + 2\beta + \phi_M$, where m is an integer, β is the phase accumulation due to propagation in the dielectric spacer layer, ϕ_M is the phase shift that takes place after reflection from the mirror and ϕ_I the one corresponding to the absorbing (thin metal film) layer. The absorber can therefore be tailored to a desired absorption wavelength predominantly by the choice of the thickness of the spacer layer. However, due to the finite electrical conductivity of metals at optical frequencies (particularly in films with thicknesses of the order of the wavelength of light), non-trivial phase changes (i.e. not limited to 0 or π), occur upon reflection from the back-reflector and front absorber and on transmission through the top metallic layer. These need to be considered when designing multi-layer, absorbing films [23, 18, 15]. While simple interference theory serves well to explain the behavior of near-perfect absorption in MIM structures, fundamentally the absorption resonance is attributed to the excitation of propagating surface plasmon polaritons (SPPs) on the metal-dielectric interfaces [6]. MIM absorber structures are usually designed to work at a specific angle of incidence and polarization state. As the angle of incidence or polarization state changes, so do the interference conditions within the structure affecting the performance of the device. For increasing angles of incidence the absorption maximum of conventional MIM absorbers blue-shifts to maintain the optimal phase shift through the dielectric and is accompanied by a decrease in absorption efficiency [15]. The sensitivity to angle of incidence can be reduced by increasing the refractive index of the spacer layer.

Extensions to three layer metal-dielectric structures in the form of one-dimensional metal-dielectric photonic crystals (MDPhC) have been suggested as multiband-absorption thin-film devices [24]. Due to the lack of a reflec-

tive substrate, however, the absorption efficiencies are only about 50% even for devices consisting of 8 layers. Two approaches to increase efficiency have been suggested. One approach relies on quasi-periodic MDPhCs, as for example Fibonnaci inspired layer sequences, with theoretical absorption efficiencies of up to 99% [25]. Secondly, a modified version incorporating a reflective substrate has recently been proposed with theoretical absorption efficiencies of up to 95% at four different wavelengths in the optical spectral range [26]. The device consists of alternating Ag and MoO_x layers with the number of absorption bands defined by the total number of slabs in MDPhC.

2.2 | Resonant absorbing and impedance matching layers

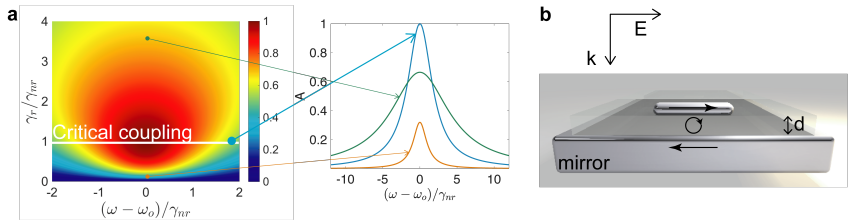

FIGURE 2 Critical-coupling in metal-spacer-nanostructures. a) diagram illustrating the light-induced dipole on a metal nanostructure and the image of this dipole on the mirror. Critical coupling occurs at a spacing thickness d where the radiation from these two induced dipoles is perfectly out-of-phase, leading to a cancellation of reflection and to perfect absorption. These two dipoles lead to a magnetic moment, indicated with the circular arrow. Light is incident on the structure (with a wavevector k and electric field E as shown in the diagram). b) Critical coupling occurs when the rates of radiative γ_r and γ_{nr} damping are equal (shown with white horizontal line). Above or below this condition, the nanostructure does not absorb perfectly, as indicated on the three cases shown to the right, where the absorption is plotted vs a (normalised) frequency detuning between the resonance frequency of the structure ω_o and that of the incident field ω.

Although NPA can be achieved using the MIM structures described in the previous section, this comes at the cost of angular sensitivity which is undesirable for many applications. Furthermore, as described above, the MIM structures typically require dielectric layers with thicknesses of the order of $\lambda/4$. Tailoring the upper layer of the structure by replacing it with a metasurface where the optical properties can be tuned to impedance match to the underlying dielectric layer and control the reflection phase provides a means to reduce the thickness of the overall structure, enhance absorption and broaden the angular response.

A material capable of light absorption and reflection (but not transmission) is analogous to a single resonator coupled to a single input channel [27]. Many theoretical approaches exist for the description of nanoscale resonators [28] although, for pedagogical reasons, we choose here to use a simple analytical (temporal) coupled–mode theory [29, 27]. According to this theory, an optical resonator supported by a mirror can be thought of as a "single port" device, namely one that can exchange energy through one interface only (given that the supporting mirror is assumed to be optically opaque) [30]. Within this framework, the interaction of the device with the radiative field is accounted for by three parameters, namely: a resonance frequency ω_o, a radiative decay rate γ_r and a non–radiative rate γ_{nr} accounting for intrinsic losses. The absorption A of the system is, in turn, given as $A = 1 - R$ and it can be explicitly written as:

$$A = \frac{4\gamma_r\gamma_{nr}}{(\gamma_r+\gamma_{nr})^2+(\omega-\omega_o)^2}, \tag{1}$$

where ω is the frequency of the incident field. Figure 2a shows how A depends on the ratio of the radiative to non-radiative decay rate and the frequency detuning of the incident field. According to this result, when the system is driven at resonance (i.e. $\omega = \omega_o$), perfect absorption ($A = 1$) occurs when the rate of radiative decay matches the one corresponding to non−radiative decay, $\gamma_r = \gamma_{nr}$: *the critical coupling condition* (white line in figure 2a) [31]. If this condition is met, energy is fed into the system at the same rate at which it is capable of dissipating it. An incoming field excites the oscillation of the resonator via radiative coupling and this resonator dissipates this power in a non-radiative way. In general, critical coupling occurs when a leaky eigenmode of a structure has equal resistive and radiative losses [32, 33] and, consequently, the realization of perfect absorption can be understood as the task of optimizing the radiative decay rate in order to match intrinsic losses in a structure.

The most widely used approach for achieving the critical coupling condition, consists of using the mirror−spacer−resonator generalization of the MIM structure discussed in the previous section (Figure 2b), where the thickness d and refractive index n of the dielectric spacer affect the optical path length at normal incidence $kd = 2\pi nd/\lambda$ (λ is the wavelength of light) which, in turn, controls the radiative-rate-matching condition described above. For a spacer thickness close to the quarter−wavelength condition (i.e. $d \approx \lambda/(4n)$) [34], the light-induced charge oscillation in the absorber layer generates an image dipole moment at the mirror, resulting in a strong magnetic moment directed perpendicular to the plane of incidence, as shown in the diagram of figure 2b. This magnetic moment produces back-scattered fields that are out of phase with respect to those produced by direct reflection from the mirror, leading to destructive interference and suppression of back-scattering [32, 14]. This phenomenon has been referred to as the excitation of a magnetic mode or magnetic resonance, and is often ascribed as the physical mechanism taking place as a consequence of critical coupling. In turn, this magnetic mode facilitates optical impedance matching and perfect absorption [11].

This mirror−spacer−resonator concept has been experimentally demonstrated numerous times in the literature, using often a regular array or random arrangement of metallic nanostructures or a metasurface as the absorbing layers, and in table 1, we show a select summary of some of these demonstrations (see also Figure 3).

In most of these cases, the critical coupling condition results in one intense absorption band. For solar energy conversion, in particular for photo-thermal applications, it is desirable to achieve broad-band absorption, ideally spanning the entire visible spectrum (an energy-rich part of solar radiation useful in applications such as photocatalysis, as we elaborate later on). One simple approach to producing broadband NPAs, consists of creating nanostructured absorption layers that posses multiple resonances.

A “dual-band" perfect absorber was demonstrated by Chen *et al.* [36], using an array of cross-shaped Au nanostructures fabricated on a MgF_2-Au support. In this structure, NPA was achieved through control over radiative damping by changes in the thickness of a MgF_2 layer (dielectric spacer). This idea can be extended further, by creating structures that support multiple and spectrally-overlapping resonances.

Metallic nanogrids can support multiple resonances, and Massiot *et al.* [42] demonstrated that this kind of structures can be employed for broadband multi−resonant light−harvesting in ultra−thin GaAs. The resonant structures are Ag grids, but the mirror−resonator spacer layer is GaAs on which the light absorption is to be maximised. A slightly more involved structure was presented by Aydin *et al.* [41], who created crossed trapezoidal arrays on top of a dielectric-mirror support. These structures can support multiple, overlapping resonances and through a judicious choice of the spacer layer and its thickness, it was possible to achieve almost complete critical-coupling yielding broadband and polarization-independent light absorption over a wavelength range extending from 400 to 700 nm, with an average absorption of 71%.

Landy *et al.* [35] demonstrated a polarization-sensitive microwave NPA incorporating two metasurfaces separated by a dielectric layer exhibiting an absorption of up to 96%. In this case the top structure acted as an impedance matching

Structure	Maximum Absorption	Frequency or Wavelength	Ref.
ERR - Wire	88%	11 GHz	[35]
Au / MgF_2 / Au disks	99%	180 THz	[11]
Au / GaAs/n-GaAs / Au grating	>95%	2.4-4.0THz	[30]
Au / In_2O_3 / Au gratings	95%	1.5-2.0μm	[32]
Au / MgF_2 / Au asymmetric cross-bars	94%	dual band:~ 3.5 - 8μm	[36]
Au / MgF_2 / Au disks	98%	825 to 1025 nm	[37]
Au / SiO_2 / Ti disks	>95%	900 nm to 1825 nm	[38]
Au/Kapton/Au H-shaped resonators	>96%	dual band: 3.30 and 3.90 μm	[39]
Au / MgF_2 / Pd nanowires	99.5%	650 nm	[12]
Au / Polymer / Ag nanocubes	99.7%	650 nm	[40]
Ag /SiO_2 / Ag nanostructures	~ 70%	broadband: 400-700 nm	[41]
Ag / GaAs / Ag nanogrid	>80%	broadband: 450-830 nm	[42]
Al / SiO_2 / Au-SnS_x and ZnO	>99%	576 - 620 nm	[34]
Au / SiO_2 / Au nano-islands	>83%	broadband 370-880 nm	[43]
Au / TiO_2 / Au nano-islands	98.9%	544 nm	[44]
Au / TiO_2 / Au nanodisks	>90%	~ 550 nm	[45]
Ag/SiO_2/Ag-SiO_2 nano-composite	>95%	dual band: 360 and 550-600 nm	[46]

TABLE 1 Select experimental demonstrations of mirror/spacer/nanostructure plasmonic near-perfect absorbers

layer and the wire array on the back surface acted as a mirror for the design polarization. Absorption in the dielectric layer dominated.

Figure 3 shows other examples where NPA has been achieved in the infrared (Fig. 3a), and visible (Fig. 3c,d) parts of the spectrum with metallic structures that support a single resonance. As demonstrated with these select examples, these structures can be constructed by using top-down lithographic approaches (Fig. 3a,d), or via bottom-up self-assembly (Fig. 3b). Figure 3c also shows that broadband NPA can be achieved when using a top nanostructure layer that consists of a distribution of particle size and geometry.

One interesting consequence of the result expressed in Equation (1) is that high absorbance can also be achieved when: (i) the resonator is not driven at resonance (i.e. when $\omega \neq \omega_o$), and also (ii) under near-critical coupling conditions (i.e. when $\gamma_r \approx \gamma_{nr}$). As examples of these two cases, it is possible to achieve an absorbance of: 80% under critical coupling but when $\omega - \omega_o = \gamma_{nr}$, and it is also possible to reach a value of 93% when at resonance and when $\gamma_r = 1.75\gamma_{nr}$ This implies that high absorbance persists despite structural imperfections in the realisation of the NPA [47, 32] and, equally as important, for materials with high intrinsic losses (i.e. large γ_{nr}, such as the case of metals like Pd and Pt), NPA can be achieved at wavelengths that are far from resonance [48].

2.3 | Quasi-two dimensional near-perfect absorbers

To reduce the volume of absorbing structures, another approach to NPA is texturing a continuous metallic surface to excite surface plasmons that dissipate energy as they propagate on a metal-dielectric boundary. One of the first near

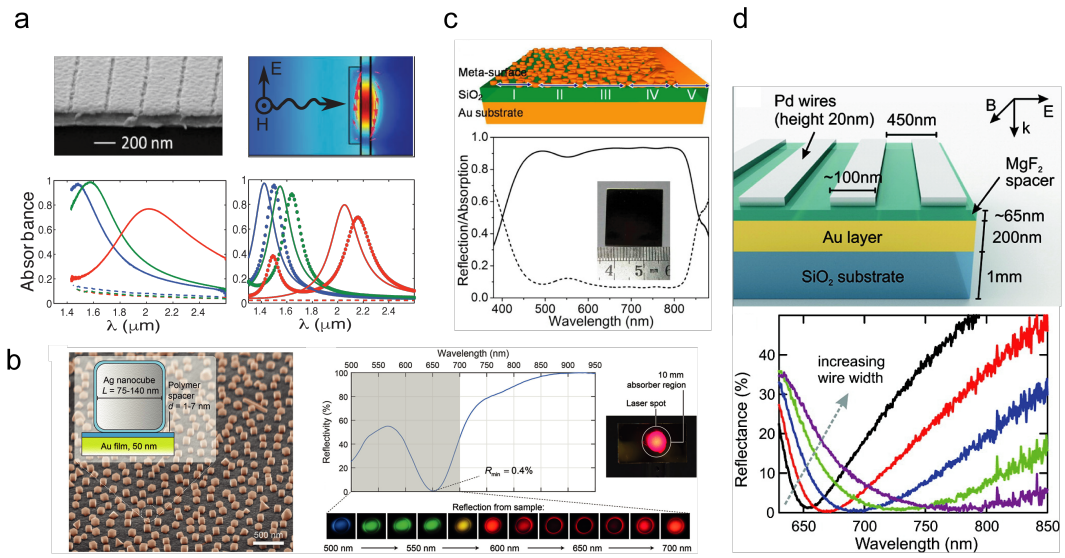

FIGURE 3 Demonstrations of near-perfect absorption of light with mirror-dielectric-plasmonic-metasurface structures. **a** Au / In_2O_3 / Au gratings that absorb at 1.5-2.0μm [32]. **b** large-area, Au/polymer/Ag nanocube absorber [40]. **c** Au/SiO_2/Au nano-island, broadband absorber [43] **d** Au/MgF_2/Pd nanowire perfect absorber [12]. The select examples demonstrate the range of frequencies (or wavelengths) at which NPA has been achieved in addition to the variety of structures employed. Reproduced with permission from respective publishers.

perfect absorbers using surface plasmon resonances was demonstrated experimentally by Davis *et al.* [49] using a silver grating with deep channels and subwavelength periodicity. Surface plasmons resonating in the grating grooves generate a reflected light wave that destructively interferes with the incident light resulting in the absorption of 84% of the incident energy, despite the grooves representing only 27% of the total surface area. They showed numerically that the absorption could be as high as 99.8% using an optimised structure. Plasmonic metasurfaces incorporating lossy, resonant cavities have also been shown to exhibit NPA in the THz region of the spectrum [50]. Annular cavities were fabricated in silicon doped so that its plasma frequency was shifted to the THz. A maximum absorption at 1.22 THz of 98.5% and a 90% absorption bandwidth of 290 GHz was experimentally demonstrated.

Another interesting approach for achieving NPA, *without* using a metal-dielectric support was demonstrated by Li *et al.* [51]. They realised narrow-band absorbers using periodic arrays of metallic nanostructures that were directly deposited on top of the mirror layer (Figure 4). The resulting structures exhibit ultra-sharp absorption resonances (with full-width at half-maximum values as low as 12 nm) with peak amplitudes exceeding 90%. In this case, the narrow line-widths originate from the excitation of surface plasmon lattice resonances, which are the physical mechanism by which control over radiative damping is achieved, enabling the realisation of critical coupling.

A theoretical study by Thongrattanasiri *et al.* [2] suggests that, in general, under the condition of critical coupling, a planar array of lossy small particles (including atoms or molecules) can exhibit perfect absorption under the additional condition that the absorption cross-section of an individual member of the array is comparable to the area of the unit cell.

Kim *et al.* [52] showed how a semiconductor metafilm constructed from optically resonant semiconductor nanostructures can be created with an optical response that mimics that of a metallic sheet. It is also possible to achieve NPA with completely non-resonant materials through mechanisms that we now discuss.

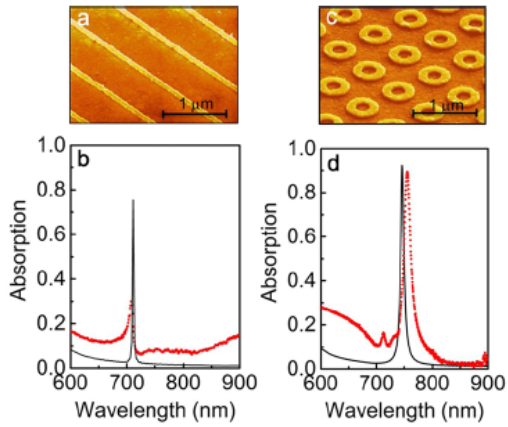

FIGURE 4 All–metal near-perfect absorber. The condition for critical coupling is achieved by the excitation of lattice resonances.

2.4 | Adiabatic focusing

Another physical mechanism that permits near–perfect absorption of light is that of adiabatic focusing [54, 55]. Adiabatic focusing can be achieved via the excitation of gap-plasmon modes in tapered metallic grooves. If the structure is designed such that variations of the (gap-plasmon) mode propagation constant are small with respect to the wavelength of light, the mode propagates, without reflection towards the narrowest region of the groove where it asymptotically stops. Energy (power) dissipation occurs in the metal throughout this propagation resulting in eventual complete absorption.

Sondergaard *et al.* [53] realised this concept by creating two-dimensional arrays of ultra-sharp convex metal grooves, where gap surface plasmon modes can be excited by scattering from sub–wavelength-sized wedges (see figure 5). This lead to broadband (450-850 nm) absorption of unpolarized light with a spectrally-averaged absorbance of 96%. Beermann *et al.* [56] demonstrated "plasmonic black nickel and palladium" materials that were constructed with two–dimensional arrays of ultra-sharp convex grooves. One of the attractive features of this approach to complete absorption of light, is the fact that this phenomenon does not rely on the excitation of an optical resonance [57].

3 | APPLICATIONS

3.1 | Structural color

The spectral dependence of strong absorption in the visible region of the spectrum has attracted considerable attraction as a mechanism for generating "structural color". This approach to coloration is well-known in the animal kingdom where multilayers and photonic crystal structures underpin iridescent colors seen in butterflies, beetles and birds [58]. Plasmonic coloration can be produced by either creating resonant structures that preferentially reflect a color associated with the particular bandwidth of the resonance. On the other hand, strong absorption over a certain spectral range permits the production of 'subtractive' color where other wavelengths are strongly reflected opening up the possibility of plasmonic color printing. The challenge is to produce bright, saturated colors by creating a relatively broad resonance with minimal reflectance at the central wavelength, but strong reflection outside the absorption band.

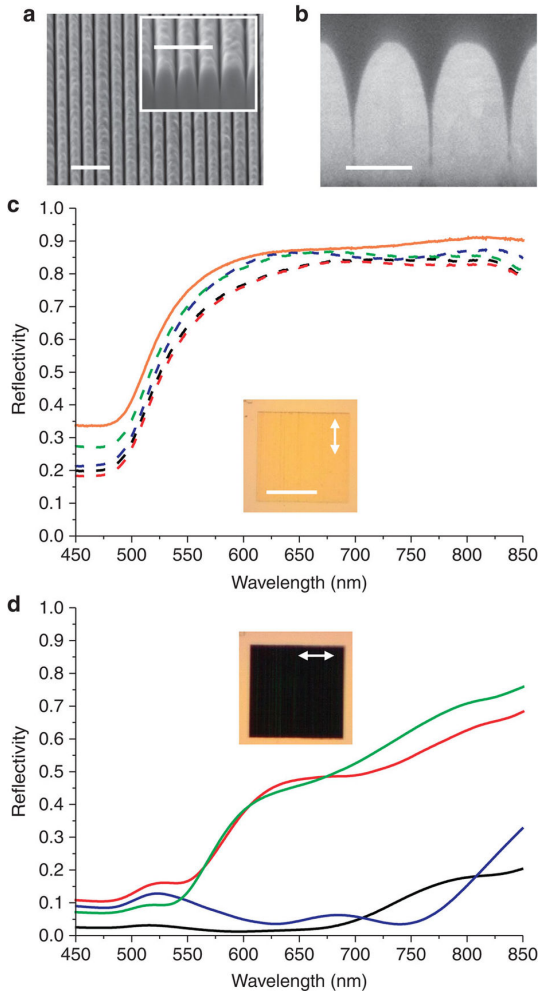

FIGURE 5 Adiabatic nanofocusing. Scanning electron microscopy images of a) an array of ultra-sharp 450-nm-deep grooves milled in gold (scale bar, 1 μm), and b) its cross-section. The grooves have a convex shape of (scale bar, 300 nm). (c,d) Reflectivity spectra of c) s-polarized (along the x axis) and d) p-polarized (along the y axis) light for convex grooves with different inclination angles (α) arranged in 1D arrays with different periods Λ, shown with green (α=14°), red (α=9°), blue (α=0°) and black (α=0°) dashed (s-polarization) and solid (p-polarization) lines (periodicity of 350 nm for the first 3 curves and 250nm for the latter one). Reflectivity spectrum for a flat gold surface is shown with a solid yellow line in c. Insets display optical microscope images (scale bar, 20 μm) of the 250-nm-period array of ultra-sharp (α=0°) 450-nm-deep grooves obtained for two orthogonal polarizations of incident light (polarization directions are indicated with arrows in the insets). Adapted from ref. [53]

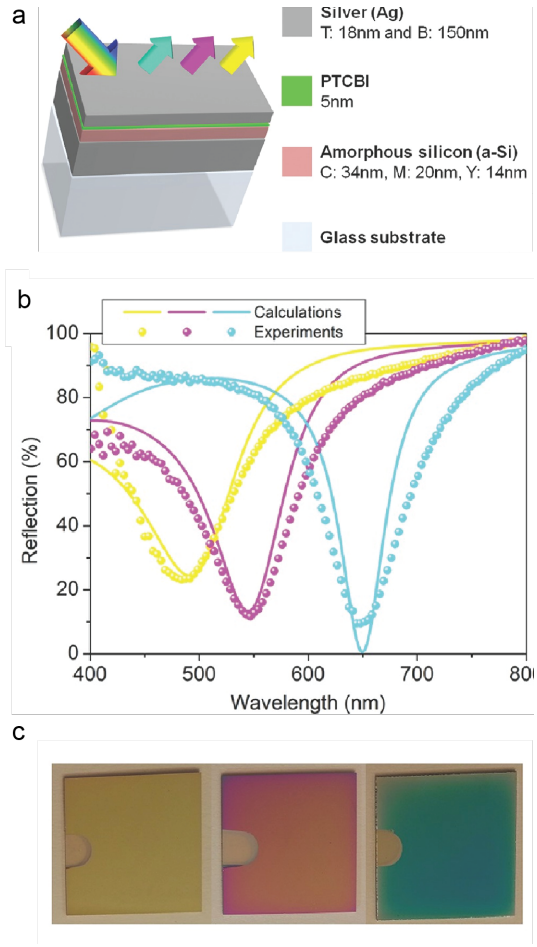

FIGURE 6 a) A schematic view of a substractive color filter. b) Calculated and measured reflection spectra at normal incidence. c) A photograph of the fabricated devices at normal incidence. Adapted from ref. [59]

Plasmonic NPAs have the capacity to satisfy these properties and are well-suited to coloration applications. Since the absorption band is geometry dependent, tuning the the structure of the absorber across a surface can be used to replicate color images or other features. Structural color provides an alternative to widely used pigments and dyes since coloration can be produced with a reduced set of materials simplifying the manufacturing process and recycling at product end-of-life. Furthermore, structural color is not 'fugitive' and does not exhibit the fading seen with conventional pigments as they age. Finally, structural color can be implemented in a single printing step permitting high-quality image production on the micron and sub-micron scale. For these reasons, plasmonic color, along with other dielectric approaches to structural coloration, is attracting widespread attention.

There is now a considerable body of work investigating plasmonic structural color and we refer the interested reader to several excellent recent review articles [60, 61, 7]. Here we focus on coloration produced by NPA achieved using plasmonic effects. A previous review of strong absorption and coloration can be found in Ji *et al.* [7].

Color resulting from interference and strong absorption in simple metal-dielectric-metal stacks is well-known [62]

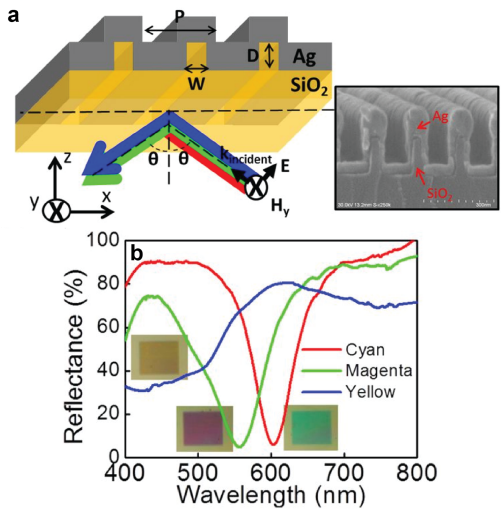

FIGURE 7 a) A schematic of the absorbing grating structure and corresponding SEM image of a fabricated device with width (W) = 45 nm, depth (D) = 160 nm, and period (P) = 180 nm b) Reflection spectra at fixed P = 180 nm and D = 170 nm demonstrating the three basic colours of the CMY colour model, cyan (C), magenta (M), and yellow (Y), with varying W = 40, 60, and 90 nm at normal incidence. Adapted from ref. [72]

and its angle-dependence has been utilized in security features for document security and anti-counterfeiting features since the 1990s [63, 64].

A significant benefit of this approach is the relatively simple fabrication with no requirement for complex nanolithography [65]. By using the resist HSQ as a dielectric and varying its thickness using grayscale electron beam lithography to produce micron scale pixels in a Ni-HSQ-Al structure Yang *et al.* [66] were able to demonstrate a relatively simple approach to full-color printing. The use of a lossy dielectric coating on the mirror has been demonstrated to produce bright, saturated coloration [67, 68, 69]. It was subsequently shown that the bandwidth of the resonance could be reduced by adding a thin layer of metal to produce a metal-insulator-metal structure [31]. Furthermore, by selecting materials with an appropriate dielectric permittivity (TiO_2 or a-Si), broad angle matching of the resonance condition could be achieved to produce colors with a wide viewing angle [31].

As described above, the next level of complexity beyond the simple metal-dielectric-metal color reflection filters is to replace the top film with a self-assembled, nano-island structure [70]. The use of a textured film as the top absorbing layer provides a means to tune the effective optical constants of the absorbing layer and, hence, to further control the resulting coloration. Replacing the dielectric film with an alumina template [71] has also been shown to increase the absorption at the resonant wavelength while reducing the sensitivity of the resulting color to the thickness of the top metal film producing more strongly saturated colors.

Direct texturing of metallic surfaces, as described earlier, can also be used to enhance absorption to produce coloration. Building on the long history of grating development, zeroth order gratings where the period of the grating is less than the wavelength of blue light have been used to demonstrate plasmonic color of various kinds. The strong angular-dependence of the resulting color, however, precludes the use of this phenomenon in most coloration applications. As a consequence, methods of patterning optically thick metal films, or metal objects, on the nanoscale are required to produce a broad gamut of saturated colors. Wu *et al.* [72] demonstrated that a Ag reflection grating with a

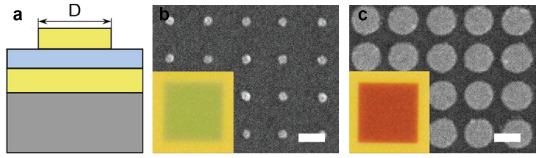

FIGURE 8 a) Schematic showing gap plasmon structure. b) and c) variations in color produced by varying the size of the top disk. Adapted from ref. [76]

subwavelength period of 180nm exhibited a strong dependence on the depth of the resonant grating (Figure 7) and strong absorption for the cyan and magenta channels, although this structure is dependent on the polarization of the incident light. Thermal effects produced by direct ps laser pulses on gold and silver surfaces created nanoparticles that produced a broad gamut of angle-robust colors [73].

A structure that has been widely investigated as a means to generate structural color consists of a mirror substrate with a layer of dielectric supporting metalic nanoparticles such as simple disks. This geometry supports 'gap plasmons' and a comprehensive review of the physics of these structures can be found in reference [74]. Sabra *et al.* [75] recently published an analytic approach for designing color filters using this geometry. By varying the size of gold disks across the surface, this approach has been used to demonstrate surface coloration (Figure 8) [76]. Subsequent, post-fabrication photo-thermal reshaping of the disks can also be performed using single-pulse laser irradiation to post-process fabricated structures as a means for color laser printing over macroscopic areas [77].

The ongoing challenge for all approaches to structural color is to produce bright, saturated colors that, furthermore, can be fabricated using an industrially scalable fabrication process and inexpensive materials [78].

3.2 | Sensing

In general, there are two detection mechanisms used in currently available LSPR sensing devices. The first mechanism operates at a single wavelength and measures the change in intensity induced by the adsorption of targeted molecules, while the second mechanism relies on the shift in spectral position of the plasmon resonance as a result of a change in the optical properties of the surrounding medium. The majority of the reported sensors using NPAs are based on the first mechanism and rely on the detection of photons that are reflected by an imperfect absorber in contrast to the nearly dark (nearly perfectly absorbing) reference measurement where only a few photons are detected. This concept possesses significant advantages over classical plasmonic sensors due to its low-background detection scheme. Since NPA-based sensors utilize intrinsic loss and interference concepts, this also permits the flexibility to develop ultra-sensitive plasmonic sensors via a wide variety of fabrication techniques such as electron beam lithography, colloidal lithography, focused ion beam writing etc. In particular, the design of NPA-based plasmonic sensors is highly flexible and can be tailored from the visible to the microwave regions of the spectrum accordingly by simply modifying the dimensions of the NPA structure and accommodating changes in the optical properties of metals. This establishes new platforms for the development of simple, cost-effective and scalable sensors for environmental monitoring and biomedical diagnostics.

Liu *et al.* [11] demonstrated for the first time using a narrow-band perfect absorber as a plasmonic sensor in the near-infrared regime using a gold disk–MgF_2–gold mirror configuration, as illustrated in Figure 9a. The MgF_2 is employed as a thin dielectric spacer layer in between the gold mirror and gold disk, while the gold disk array ensures that the NPA structure is independent of polarization and functions as a wide-angle absorber. A change in refractive

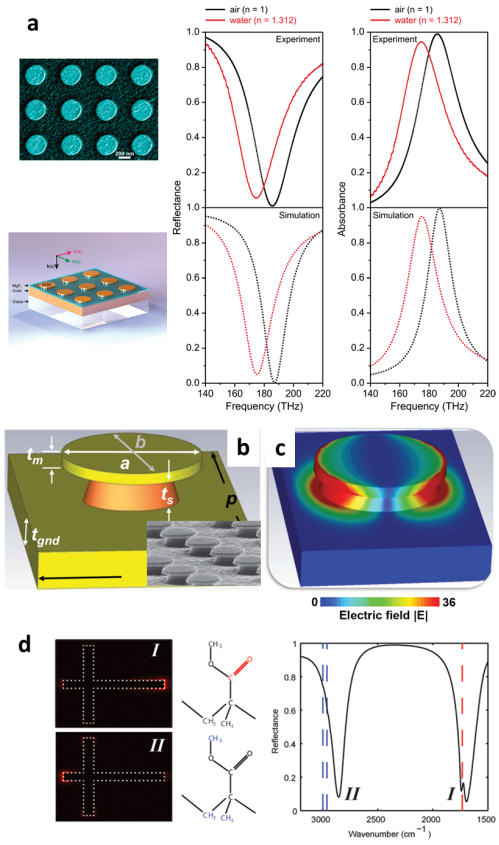

FIGURE 9 a) Left: SEM image and illustration of the perfect absorber consisting of gold nanodisk-MgF_2-gold mirror. Right: Experimental tuning of the optical spectra by altering the surrounding medium from air to water. b)A unit cell of mushroom-capped NPA with exposed dielectric spacer.Inset: Side-view SEM image of the mushroom-capped NPA. c) Simulated amplitude of the electric field exhibited by the mushroom-capped NPA at the resonance wavelength. d)Left: Simulated near-field intensity enhancement of two different excited modes. Right: SEIRA spectroscopy (Reflectance spectrum) of 4nm PMMA on the NPA.Characteristic vibrational stretches of C=O and C-H are indicated by the red and blue dashed line respectively.

index of the liquid above the disks of dn (air and water in Figure 9a) produces a relative intensity change $dI(\lambda)/I(\lambda)$ at a fixed wavelength λ . The figure of merit FOM* introduced by Becker *et al.* [79] is defined as FOM* = max $|dI(\lambda)/dn/I(\lambda)|$, where λ is chosen at a corresponding maximum value of FOM*. With this NPA configuration, they experimentally achieved a FOM* of approximately 87 by detecting intensity changes accompanying different local dielectric materials on the surface of the sample. A FOM* value is almost four times larger than that of plasmonic sensors consisting of simple gold nanorods was obtained.

Using an analogous concept Tittl *et al.* [12] presented an NPA design based on palladium nanowires that exhibits NPA at visible wavelengths for hydrogen gas detection (see Figure 3). Palladium was selected because of its strong change in optical properties upon hydrogen absorption, where the optical change is induced by a phase transition from metal to metal hydride that results in an expansion of the palladium lattice. The structure consisting of palladium nanowires, an MgF_2 spacer layer and a gold mirror exhibits a reflectance of <0.5% and zero transmittance at 650 nm. The reflectance dip can be easily tuned by varying the widths of the palladium wires. In addition to improving the change in reflectivity by one order of magnitude, they also demonstrated the capacity to detect hydrogen concentrations down to 0.5% with a response time in the range of seconds reliably and reproducibly. At this point, it is worth highlighting the flexibility and simplicity of designing appropriate NPA-based devices for a wide variety of sensing applications by manipulating the constituents of the final NPA structure (e.g. palladium for hydrogen gas sensing).

In the work described above, only the top surface of the metal-dielectric-mirror sensor is accessible to gas or liquid analytes. Although the spacer layer between the resonator and mirror exhibits strong electromagnetic field confinement, the region is considered inaccessible and generally neglected. To gain access to this region, Bhattarai *et al.* [80] fabricated a large area, low cost, uniform, mushroom-capped NPA, where the dielectric spacer is partially etched by a reactive-ion-etch process (Figure 9b). With a mushroom-like configuration, the local confinement in between the mirror and resonator is exposed and accessible to target molecules for sensing purposes. Additionally, a strong localization of the resonant electric field exists under the edge of the top disc as depicted in Figure 9c, thereby making this region much more sensitive to changes in refractive index compared to the top surface region. Subsequently, a Fabry-Pérot model was developed to reinterpret the perfect absorption behavior and the augmented theoretical Q-factor is shown to improve the FOM* to a maximum value of 179.23, which lies in the upper limit of current reported values.

In contrast to typical periodic structures that are fabricated by lithographic methods, zero-reflectance metafilms consisting of an ultrathin layer of metal nanoparticles, self-assembled with the aid of linker molecules (APTES) onto a reflective silicon layer, were presented recently by Huang *et al.* [81]. Despite the absence of well-defined periodic structures, the zero-reflectance metafilms exhibit near perfect absorption of more than 99.5% over a wide range of incidence angles in the visible range. As demonstrated in this work, the enhanced absorption is a result of a Fano resonance that originates from the coupling between the LSPR of individual plasmonic nanoparticles and the continuum spectrum of silicon. These zero-reflectance metafilms are highly favorable for ultrasensitive molecular sensing, due to the fact that Fano resonant nanostructures are inherently sensitive to changes in the surrounding medium, where small changes in the local optical environment can result in dramatic changes in the line shape or spectral shifts. In addition, the dip in the reflectance that corresponds to near perfect absorption is an indication of an “anti-resonance” behavior of the Fano resonance and hence possesses enhanced sensitivity to any change in the surrounding environment. The overall intensity of such zero-reflectance films is, however, low and is deemed inappropriate for small spectral shifts. In terms of practicality, these films can be readily fabricated via self-assembly method and offer real opportunities for developing cost-efficient sensors for a variety of applications.

Nevertheless, one of the most significant limitations of NPA-based sensing mentioned so far is the relatively narrowband response that results from the resonances of small metal nanoparticles. NPA devices with multiple bands

are desirable for biochemical sensing, in particular in the field of mid-IR spectroscopy (e.g. SEIRA spectroscopy), where it is of significance for simultaneously monitoring the multiple spectral fingerprint regions that are characteristic to different chemical or biological target molecules. To overcome this limitation, Chen *et al.* [36] introduced a dual-band perfect absorber using the gold nanocross structure shown in Figure 9d, placed on top of a MgF_2 dielectric spacer layer supported by an underlying gold mirror. Two absorption bands (separated by 3μm) with a maximum absorption of 94% were demonstrated experimentally by breaking the symmetry using a cross structure. In addition to the tunability of these two bands throughout the mid-IR region, the associated resonances of the NPA structure also create a large near-field enhancement, ideal for surface-enhanced infrared absorption spectroscopy (SEIRA) applications. Based on the two tunable resonances, they demonstrated the use of the designed NPA device to simultaneously monitor widely separated multiple molecular vibrational modes (Figure 9d) using a 4nm PMMA film as the model analyte. NPA devices with triple- and four-bands have also been reported for sensing purposes [82, 83, 84, 85]. For example, Liu et al. successfully designed a NPA structure consisting of a plasmonic nanocavity absorber that possesses the capability for a four-band near-perfect absorption for multispectral biosensors [85] and fabricated a triple-band hybrid plasmonic-photonic absorber with a maximum FOM* of 1337 for refractive sensing in the visible and near-infrared regions [84].

3.3 | Photocatalysis

Materials that can harness radiant energy and transform it into chemical potential energy are of great importance to the field of photocatalysis [89], where one of the grand challenges is enabling a solar-powered chemical manufacturing industry [90, 91]. One of the particular aspects of metal nanostructures is that non−radiative power dissipation can occur via a Landau decay process which results in transient populations of energetic charge carriers referred to as hot carriers (electrons and holes) [92, 93]. One approach for capturing these energetic charge carriers is to create metal-semiconductor contacts, which can lead to Schottky junctions, where electrons generated in a metal can escape into the (n-type) semiconductor if their energy is higher than the energy barrier at the interface and their momentum lies within the escape cone [92, 93]. While the exact mechanism for hot-carrier generation and emission with metal nanostructures is still a subject of intense debate [94], it is clear that absorption of electromagnetic energy is of fundamental importance in this process. In this aspect, plasmonic near-perfect absorption of light has been experimentally demonstrated to increase the efficiency of hot-carrier photo-chemistry [45, 44, 95, 86, 87].

Fang *et al.* [45] reported plasmon-induced photocurrent generation in mirror/TiO_2/gold nanodisks structures. These structures support multiple resonance peaks due to the hybridization of localized surface plasmons in the nanodisks and Fabry-Pérot cavity modes caused by reflections between the mirror and the nanostructured layer. These hybrid modes lead to peak absorbance $> 90\%$ in the visible range of the electromagnetic spectrum. Due to the increased absorption of electromagnetic energy, the authors observed enhanced photo-currents that were between 2 to 10-fold greater than those obtained with similar structures that lacked the mirror support. The observed enhancements correlated well with those wavelengths that correspond to constructive Fabry-Pérot interference maxima overlapping with the nanodisk layer.

Ng *et al.* [44] demonstrated that a simple structure consisting of an Au mirror supporting a thin TiO_2 film loaded with a monolayer of Au nanoparticles can exhibit $> 90\%$ absorption of light in the visible (Figure 10a). The bandwidth of the absorption was relatively broad, enabling these systems to more efficiently harvest radiant energy for the generation of hot-carrier photo-currents. The increased light absorption resulted in a 40-fold enhancement of the measured photo-current, when these materials where employed as anodes in a photo-electrochemical cell. The concept was later extended by Xiao *et al.* [86] who demonstrated that these near-perfect absorbers can be used for the light-driven

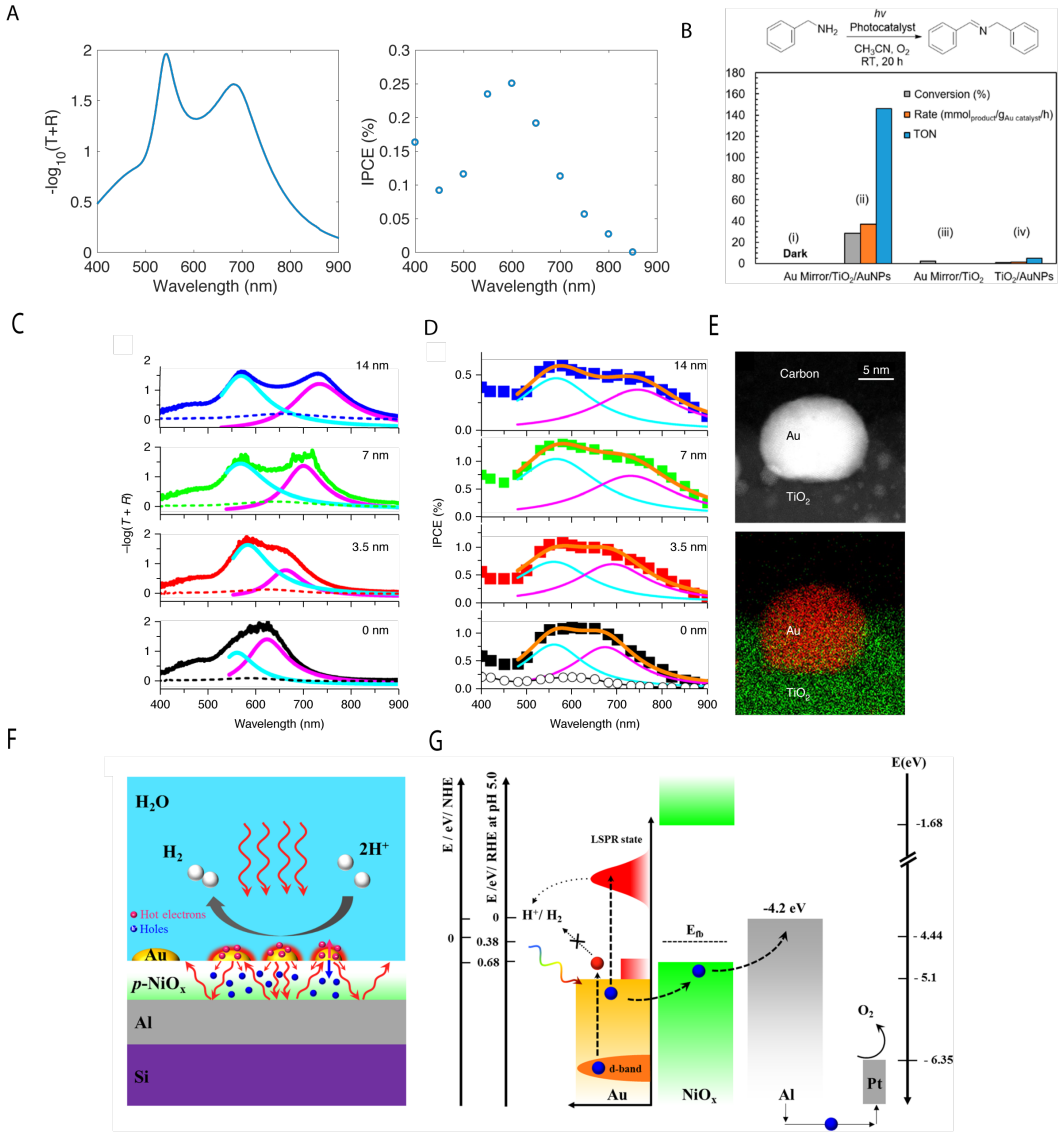

FIGURE 10 Applications in photocatalysis: a: Measured absorption spectrum of a Au/TiO_2/Au - nanoisland film and its associated IPCE spectrum for photocurrent generation [44]. b: Application of the same system for the synthesis of iminium intermediates [86]. c:Absorption spectra of Au/TiO_2/Au - nanoisland film structures with varying Au-NP inlaid depths and d: corresponding IPCE spectra. e: (top) Cross-section of a single Au NP with an "inlaid" depth of approximately 7 nm. (bottom) Energy-dispersive X-ray map of the inlaid structure. [87] f: Diagram of a Al/NiO_x/Au nanoisland structure for photocatlysis that does not use a Schottky barrier [88]

preparation of chemically-reactive intermediates that are useful in the chemical manufacturing industry. Due to the enhanced light-absorption, they reported a 29-fold increase in the percent conversion of reactant molecules into the target product, with almost 100% chemical selectivity (Figure 10b).

Shi *et al.* [87] demonstrated that when there is strong coupling between the Fabry-Pérot cavity modes and the localized surface plasmon resonances, polariton splitting takes place and is manifested as: (i) an avoided crossing in an energy dispersion curve of the coupled system [96] and (ii) spectral doublets in the absorption spectra which account for the "broadband" action observed in a similar system reported by Ng *et al.* (compare Figure 10a and c). Under strong coupling, the excited states of the system are no longer localized plasmons or Fabry-Pérot resonances, but hybrid modes which posses unique and distinct properties. Due to strong coupling, the authors were able to observe an 11-fold increase in the incident photon-to-current conversion efficiency (with respect to a control structure, with no mirror) and, furthermore, a 1.5 times increase in the internal quantum efficiency. One important aspect of their work was the partial immersion of Au nanoislands into the semiconductor, which is known to increase the efficieny of hot-carrier collection [97].

Interestingly, Robatjazi *et al.* [88] demonstrated that it is also possible to create absorber structures for photocatalysis *without* the need for a nanoparticle-semiconductor Schottky junction. This is important as it widens the possible material combinations that can be used for NPA–enabled photochemistry.

3.4 | Opto-electronics

NPA can be used to greatly enhance and extend the performance of hot-electron injection based photodetectors. Silicon Schottky photodetectors, in particular [98, 99, 100, 101] are of a great interest as they combine the cost efficiency of a conventional CMOS technology and an ability to sense light in the infrared region of the spectrum.

The principle underlying photodetection beyond the semiconductor bandgap is very similar to photocatalysis as described in the previous section. The excited surface plasmon decays non-radiatively in the metal resulting in hot-electron generation that can overcome a Schottky barrier and contribute to the photocurrent. This process is, however, less efficient than common PIN photodetectors. The responsivity of silicon-based infrared photodetectors, therefore, does not exceed approximately 100 μA/W [102, 103]. The absorption can be enhanced by a substantial increase in the metal thickness, but this leads to a significant decrease in the hot-electron injection probability. It is, therefore, essential to maintain a metal thickness of the order of the hot-electron diffusion length.

The use of NPA structures described above, however, permits a substantial increase in the non-radiative absorption of surface plasmons in the metal layer without increasing its thickness. As recently reported by Li and Valentine [104], a simple perfect absorber structure consisting of one-dimensional metal stripes permits near unity absorption with appropriate design of the plasmonic grating (see Figure 11). The Fabry-Pérot resonance appears in the cavity formed by the top and bottom metal stripes. Overlapping this resonance with the plasmonic resonance of the stripes greatly increases the absorption in the metal. Note that the metal thickness in the reported paper was only 15 nm, which guaranteed a high hot-electron diffusion probability into the semiconductor substrate. The maximum responsivity of the photodetector was measured at an impressive 3.37 mA/W. It should also be mentioned that, although the best performance is achieved when the cavity and plasmonic resonances perfectly coincide, this photodetector also provides a relatively broadband absorption that opens up opportunities to use this detector in fields outside applications in near-IR telecommunications.

The utilization of perfect absorbers is not limited to metal-only based photodetectors. In fact, transparent conducting oxides (TCO) such as ITO [103, 106] or AZO [107, 108, 109] can also be used to create effective photodetectors. A fully-planar perfect absorber incorporating TCO thin films was demonstrated by Zhan *et al.* [105]. The structure

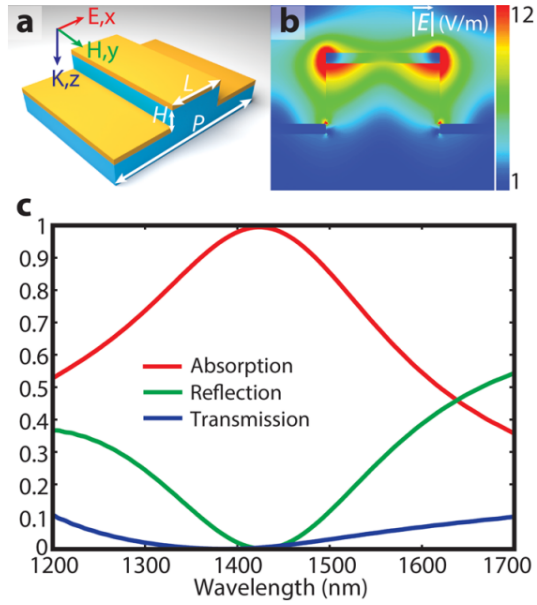

FIGURE 11 Schematic representation of a simple perfect absorber structure based on 1D metal stripes on silicon substrate a) The normalised electric field distribution at TM-polarised illumination b) Simulated optical characteristics of the structure c) Reprinted with permission from [104].

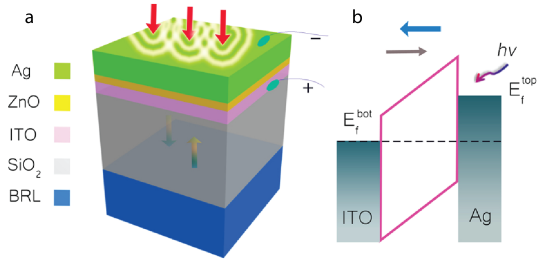

FIGURE 12 Schematic representation of planar transparent conducting oxide based photodetector a). Band diagram of ITO-ZnO-Ag photodetector b). Reprinted with permission from [105].

consists of a semi-transparent Ag layer and transparent ZnO, ITO, SiO_2 films with a back reflector located underneath (see Figure 12a). The photodetection occurs in the first three layers, while the other two are added to form a perfect absorber structure. ZnO in this structure serves as an insulator, forming Schottky barriers with both the Ag and ITO films (see Figure 12b). The hot electrons are generated at both the ITO-ZnO and ZnO-Ag interfaces and injected into ZnO layer. The drawback of this structure is associated with reverse direction of these electron flows. The resulting photocurrent is, thus, a difference between counter-propagating photocurrents. Nevertheless, the structure reported to exhibit an impressive 60 mA/W photocurrent at 1550 nm wavelength.

The perfect absorber photodetector configuration significantly enhances the performance of photodetectors. It can potentially open up substantial opportunities for the development of low cost silicon-based CMOS-compatible infrared photodetectors. These detectors can be used in "on-chip" optical interconnects in future optoelectronic integrated circuits.

4 | OUTLOOK AND CONCLUSION

In terms of future developments in the field, the converse of the sensing capability of NPA will be utilizing active materials to facilitate the creation of wavelength-tunable devices. NPA can also enable novel effects such as the control over strong light-matter interactions. In this context, metal–dielectric–absorber structures can act as optical cavities that simultaneously have a greatly enhanced local electromagnetic field [110] and enable control over the energy-momentum relationship of the hybrid light-matter states (polaritons) that result from strong coupling. In fact, there is a growing number of experimental demonstrations in this regard, which to-date include strong coupling to vibrational modes [36], quantum wells [111] and near-perfect energy feeding into polariton states [33]. Integration of NPA structures into Si will permit monolithically integrated color sensing, minizing cross-talk and enabling much smaller pixel sizes in future imaging systems. The fact that good absorbers are also good emitters provides a new avenue for tailoring thermal radiation [112]. Further progress in the field will be enabled by advances in scalable approaches to nanofabrication including bottom-up solution processing of materials and fabrication on flexible substrates to permit large-scale conformal coating of arbitrary surfaces.

5 | ACKNOWLEDGEMENTS

The authors acknowledge the financial support of the Australian Research Council through its Future Fellowships (FT140100514) and Discovery Projects (DP160100983) schemes. C.N. would like to acknowledge the support from Alexander von Humboldt Foundation.

REFERENCES

[1] P. Yu, L. V. Besteiro, Y. Huang, J. Wu, L. Fu, H. H. Tan, C. Jagadish, G. P. Wiederrecht, A. O. Govorov, Z. Wang, *Adv. Opt. Mater.* **2019**, *7*, 1800995.

[2] S. Thongrattanasiri, F. H. L. Koppens, F. J. García de Abajo, *Phys. Rev. Lett.* **2012**, *108*, 047401.

[3] F. J. García de Abajo, *Rev. Mod. Phys.* **2007**, *79*, 1267.

[4] H. A. Macleod, H. A. Macleod, *Thin-film optical filters*, CRC Press, **2010**.

[5] C. M. Watts, X. Liu, W. J. Padilla, *Adv. Mater.* **2012**, *24*, OP98.

[6] Y. Cui, Y. He, Y. Jin, F. Ding, L. Yang, Y. Ye, S. Zhong, Y. Lin, S. He, *Laser Photonics Rev.* **2014**, *8*, 495.

[7] C. Ji, K.-T. Lee, T. Xu, J. Zhou, H. J. Park, L. J. Guo, *Adv. Opt. Mater.* **2017**, *5*, 1700368.

[8] O. S. Heavens, *Optical properties of thin solid films*, Courier Corporation, **1991**.

[9] S.-Y. Lien, D.-S. Wuu, W.-C. Yeh, J.-C. Liu, *Sol. Energy Mater. Sol. Cells* **2006**, *90*, 2710.

[10] M. S. Ünlü, S. Strite, *J. Appl. Phys.* **1995**, *78*, 607.

[11] N. Liu, M. Mesch, T. Weiss, M. Hentschel, H. Giessen, *Nano Lett.* **2010**, *10*, 2342.

[12] A. Tittl, P. Mai, R. Taubert, D. Dregely, N. Liu, H. Giessen, *Nano Lett.* **2011**, *11*, 4366.

[13] Z. Fang, Y.-R. Zhen, L. Fan, X. Zhu, P. Nordlander, *Phys. Rev. B* **2012**, *85*, 245401.

[14] H.-T. Chen, *Opt. Express* **2012**, *20*, 7165.

[15] Z. Li, S. Butun, K. Aydin, *ACS Photonics* **2015**, *2*, 183.

[16] W. W. Salisbury, *US Patent 2599944A* **1952**.

[17] H. Shin, M. F. Yanik, S. Fan, R. Zia, M. L. Brongersma, *Appl. Phys. Lett.* **2004**, *84*, 4421.

[18] S. Shu, Z. Li, Y. Y. Li, *Opt. Express* **2013**, *21*, 25307.

[19] M. Yan, *J. Opt.* **2013**, *15*, 025006.

[20] J. R. Tischler, M. S. Bradley, V. Bulović, *Opt. Lett.* **2006**, *31*, 2045.

[21] W. Streyer, S. Law, G. Rooney, T. Jacobs, D. Wasserman, *Opt. Express* **2013**, *21*, 9113.

[22] H.-T. Chen, *Opt. Express* **2012**, *20*, 7165.

[23] B. J. Lee, Z. Zhang, *J. Appl. Phys.* **2006**, *100*, 063529.

[24] J. Yu, Y. Shen, X. Liu, R. Fu, J. Zi, Z. Zhu, *J. Phys.: Condens. Matter* **2004**, *16*, L51.

[25] J. Dong, G. Liang, Y. Chen, H. Wang, *Opt. Express* **2006**, *14*, 2014.

[26] W. Wang, Y. Cui, Y. He, Y. Hao, Y. Lin, X. Tian, T. Ji, S. He, *Opt. Lett.* **2014**, *39*, 331.

[27] H. Haus, *Waves and fields in optoelectronics*, Prentice Hall, **1984**.

[28] C. Sauvan, J. P. Hugonin, I. S. Maksymov, P. Lalanne, *Phys. Rev. Lett.* **2013**, *110*, 237401.

[29] S. Fan, W. Suh, J. D. Joannopoulos, *J. Opt. Soc. Am. A* **2003**, *20*, 569.

[30] J.-M. Manceau, S. Zanotto, I. Sagnes, G. Beaudoin, R. Colombelli, *Appl. Phys. Lett.* **2013**, *103*, 091110.

[31] K.-T. Lee, S. Seo, L. J. Guo, *Adv. Opt. Mater.* **2015**, *3*, 347.

[32] C. Wu, B. Neuner, G. Shvets, J. John, A. Milder, B. Zollars, S. Savoy, *Phys. Rev. B* **2011**, *84*, 075102.

[33] S. Zanotto, F. P. Mezzapesa, F. Bianco, G. Biasiol, L. Baldacci, M. S. Vitiello, L. Sorba, R. Colombelli, A. Tredicucci, *Nat. Phys.* **2014**, *10*, 830.

[34] C. Hägglund, G. Zeltzer, R. Ruiz, I. Thomann, H.-B.-R. Lee, M. L. Brongersma, S. F. Bent, *Nano Lett.* **2013**, *13*, 3352.

[35] N. I. Landy, S. Sajuyigbe, J. J. Mock, D. R. Smith, W. J. Padilla, *Phys. Rev. Lett.* **2008**, *100*, 207402.

[36] K. Chen, R. Adato, H. Altug, *ACS Nano* **2012**, *6*, 7998.

[37] R. Walter, A. Tittl, A. Berrier, F. Sterl, T. Weiss, H. Giessen, *Adv. Opt. Mater.* **2015**, *3*, 398.

[38] F. Ding, J. Dai, Y. Chen, J. Zhu, Y. Jin, S. I. Bozhevolnyi, *Sci. Rep.* **2016**, *6*, 39445.

[39] Z. H. Jiang, S. Yun, F. Toor, D. H. Werner, T. S. Mayer, *ACS Nano* **2011**, *5*, 4641.

[40] G. M. Akselrod, J. Huang, T. B. Hoang, P. T. Bowen, L. Su, D. R. Smith, M. H. Mikkelsen, *Adv. Mater.* **2015**, *27*, 8028.

[41] K. Aydin, V. E. Ferry, R. M. Briggs, H. A. Atwater, *Nat. Commun.* **2011**, *2*, 517.

[42] I. Massiot, N. Vandamme, N. Bardou, C. Dupuis, A. Lemaître, J.-F. Guillemoles, S. Collin, *ACS Photonics* **2014**, *1*, 878.

[43] Z. Liu, X. Liu, S. Huang, P. Pan, J. Chen, G. Liu, G. Gu, *ACS Appl. Mater. Interfaces* **2015**, *7*, 4962.

[44] C. Ng, J. Cadusch, S. Dligatch, A. Roberts, T. J. Davis, P. Mulvaney, D. E. Gomez, *ACS Nano* **2016**, *10*, 4704.

[45] Y. Fang, Y. Jiao, K. Xiong, R. Ogier, Z. Yang, S. Gao, A. Dahlin, M. Käll, *Nano Lett.* **2015**, *15*, 4059.

[46] M. K. Hedayati, A. U. Zillohu, T. Strunskus, F. Faupel, M. Elbahri, *Appl. Phys. Lett.* **2014**, *104*, 041103.

[47] A. Tittl, M. G. Harats, R. Walter, X. Yin, M. Schäferling, N. Liu, R. Rapaport, H. Giessen, *ACS Nano* **2014**, *8*, 10885.

[48] T. U. Connell, G. O. Bonin, C. D. Easton, E. Della Gaspera, A. S. R. Chesman, T. J. Davis, D. E. Gómez, *ACS Appl. Energy Mater.* **2019**, *2*, 1155.

[49] T. Davis, S. Mayo, B. Sexton, *Opt. Commun.* **2006**, *267*, 253.

[50] W. Withayachumnankul, C. M. Shah, C. Fumeaux, B. S.-Y. Ung, W. J. Padilla, M. Bhaskaran, D. Abbott, S. Sriram, *ACS Photonics* **2014**, *1*, 625.

[51] Z. Li, S. Butun, K. Aydin, *ACS Nano* **2014**, *8*, 8242.

[52] S. J. Kim, J. Park, M. Esfandyarpour, E. F. Pecora, P. G. Kik, M. L. Brongersma, *Nano Lett.* **2016**, *16*, 3801.

[53] T. Søndergaard, S. M. Novikov, T. Holmgaard, R. Eriksen, J. Beermann, Z. Han, K. Pedersen, S. I. Bozhevolnyi, *Nat. Commun.* **2012**, *3*, 969.

[54] A. J. Babadjanyan, N. L. Margaryan, K. V. Nerkararyan, *J. Appl. Phys.* **2000**, *87*, 3785.

[55] M. I. Stockman, *Phys. Rev. Lett.* **2004**, *93*, 137404.

[56] J. Beermann, R. Eriksen, T. Holmgaard, K. Pedersen, S. I. Bozhevolnyi, *Sci. Rep.* **2014**, *4*, 6904.

[57] Z. Li, E. Palacios, S. Butun, H. Kocer, K. Aydin, *Sci. Rep.* **2015**, *5*, 15137.

[58] S. Kinoshita, S. Yoshioka, *ChemPhysChem* **2005**, *6*, 1442.

[59] K.-T. Lee, S. Seo, J. Y. Lee, L. J. Guo, *Adv. Mater.* **2014**, *26*, 6324.

[60] Y. Gu, L. Zhang, J. K. W. Yang, S. P. Yeo, C.-W. Qiu, *Nanoscale* **2015**, *7*, 6409.

[61] T. Lee, J. Jang, H. Jeong, J. Rho, *Nano Convergence* **2018**, *5*, 1.

[62] L. N. Hadley, D. M. Dennison, *J. Opt. Soc. Am.* **1947**, *37*, 451.

[63] R. W. Phillip, A. F. Bleikolm, *Appl. Opt.* **1996**, *35*, 5529.

[64] R. L. van Renesse, *Optical Document Security 3rd ed.*, Artech House, Boston, **2004**.

[65] A. Ghobadi, H. Hajian, B. Butun, E. Ozbay, *ACS Photonics* **2018**, *0*, 4203.

[66] Z. Yang, Y. Chen, Y. Zhou, Y. Wang, P. Dai, X. Zhu, H. Duan, *Adv. Opt. Mater.* **2017**, *5*, 1700029.

[67] M. A. Kats, S. J. Byrnes, R. Blanchard, M. Kolle, P. Genevet, J. Aizenberg, F. Capasso, *Appl. Phys. Lett.* **2013**, *103*, 101104.

[68] M. A. Kats, R. Blanchard, P. Genevet, F. Capasso, *Nat. Mater.* **2013**, *12*, 20.

[69] M. A. Kats, D. Sharma, J. Lin, P. Genevet, R. Blanchard, Z. Yang, M. M. Qazilbash, D. Basov, S. Ramanathan, F. Capasso, *Appl. Phys. Lett.* **2012**, *101*, 221101.

[70] A. Leitner, Z. Zhao, H. Brunner, F. R. Aussenegg, A. Wokaun, *Appl. Opt.* **1993**, *32*, 102.

[71] J. Xue, Z.-K. Zhou, Z. Wei, R. Su, J. Lai, J. Li, C. Li, T. Zhang, X.-H. Wang, *Nat. Commun.* **2015**, *6*, 8906.

[72] Y.-K. R. Wu, A. E. Hollowell, C. Zhang, L. J. Guo, *Sci. Rep.* **2013**, *3*, 1194.

[73] J.-M. Guay, A. Calà Lesina, G. Côté, M. Charron, D. Poitras, L. Ramunno, P. Berini, A. Weck, *Nat. Commun.* **2017**, *8*, 16095.

[74] F. Ding, Y. Yang, R. Deshpande, S. I. Bozhevolnyi, *Nanophotonics* **2018**, *7*, 1129.

[75] W. Sabra, S. I. Azzam, M. Song, M. Povolotskyi, A. H. Aly, A. V. Kildishev, *Opt. Lett.* **2018**, *43*, 4815.

[76] A. S. Roberts, A. Pors, O. Albrektsen, S. I. Bozhevolnyi, *Nano Lett.* **2014**, *14*, 783.

[77] X. Zhu, C. Vannahme, E. Højlund-Nielsen, N. A. Mortensen, A. Kristensen, *Nat. Nanotechnol.* **2015**, *11*, 325.

[78] E. Højlund-Nielsen, J. Clausen, T. Mäkela, L. H. Thamdrup, M. Zalkovskij, T. Nielsen, N. Li Pira, J. Ahopelto, N. A. Mortensen, A. Kristensen, *Adv. Mater. Technologies* **2016**, *1*, 1600054.

[79] J. Becker, A. Trügler, A. Jakab, U. Hohenester, C. Sönnichsen, *Plasmonics* **2010**, *5*, 161.

[80] K. Bhattarai, Z. Ku, S. Silva, J. Jeon, J. O. Kim, S. J. Lee, A. Urbas, J. Zhou, *Adv. Opt. Mater.*, *3*, 1779.

[81] F. Huang, S. Drakeley, M. G. Millyard, A. Murphy, R. White, E. Spigone, J. Kivioja, J. J. Baumberg, *Adv. Opt. Mater.* **2015**, *4*, 328.

[82] Y. Li, B. An, S. Jiang, J. Gao, Y. Chen, S. Pan, *Opt. Express* **2015**, *23*, 17607.

[83] B.-X. Wang, G.-Z. Wang, T. Sang, *J. Phys. D: Appl. Phys.* **2016**, *49*, 165307.

[84] Z. Liu, M. Yu, S. Huang, X. Liu, Y. Wang, M. Liu, P. Pan, G. Liu, *J. Mater. Chem. C* **2015**, *3*, 4222.

[85] Z.-Q. Liu, H.-B. Shao, G.-Q. Liu, X.-A. Liu, H.-Q. Zhou, Y. Hu, X.-n. Zhang, Z.-j. Cai, G. Gu, *Appl. Phys. Lett.* **2014**, *104*, 81116.

[86] Q. Xiao, T. U. Connell, J. Cadusch, A. Roberts, A. S. R. Chesman, D. Gomez, *ACS Catalysis* **2018**, *8*, 10331.

[87] X. Shi, K. Ueno, T. Oshikiri, Q. Sun, K. Sasaki, H. Misawa, *Nat. Nanotechnol.* **2018**, 953.

[88] H. Robatjazi, S. M. Bahauddin, C. Doiron, I. Thomann, *Nano Lett.* **2015**, 6155.

[89] Y. Tian, F. P. García de Arquer, C.-T. Dinh, G. Favraud, M. Bonifazi, J. Li, M. Liu, X. Zhang, X. Zheng, M. G. Kibria, S. Hoogland, D. Sinton, E. H. Sargent, A. Fratalocchi, *Adv. Mater.* **2017**, *29*, 1701165.

[90] X. Meng, L. Liu, S. Ouyang, H. Xu, D. Wang, N. Zhao, J. Ye, *Adv. Mater.* **2016**, 6781.

[91] D. M. Schultz, T. P. Yoon, *Science* **2014**, *343*, 1239176.

[92] M. L. Brongersma, N. J. Halas, P. Nordlander, *Nat. Nanotechnol.* **2015**, *10*, 25.

[93] M. Moskovits, *Nat. Nanotechnol.* **2015**, *10*, 6.

[94] J. B. Khurgin, *Nat. Nanotechnol.* **2015**, *10*, 2.

[95] C. Ng, L. W. Yap, A. R. W. Cheng, D. E. Gómez, *Adv. Funct. Mater* **2016**, *27*, 1604080.

[96] C. Hägglund, G. Zeltzer, R. Ruiz, A. Wangperawong, K. E. Roelofs, S. F. Bent, *ACS Photonics* **2016**, *3*, 456.

[97] M. W. Knight, Y. Wang, A. S. Urban, A. Sobhani, B. Y. Zheng, P. Nordlander, N. J. Halas, *Nano Lett.* **2013**, *13*, 1687.

[98] E. Panchenko, J. J. Cadusch, T. D. James, A. Roberts, *ACS Photonics* **2016**, *3*, 1833.

[99] E. Panchenko, J. J. Cadusch, O. Avayu, T. Ellenbogen, T. D. James, D. Gómez, A. Roberts, *Adv. Mater. Technol.* **2018**, *3*, 1700196.

[100] B. Desiatov, I. Goykhman, N. Mazurski, J. Shappir, J. B. Khurgin, U. Levy, *Optica* **2015**, *2*, 335.

[101] A. Akbari, R. N. Tait, P. Berini, *Opt. Express* **2010**, *18*, 8505.

[102] A. Sobhani, M. W. Knight, Y. Wang, B. Zheng, N. S. King, L. V. Brown, Z. Fang, P. Nordlander, N. J. Halas, *Nat. Commun.* **2013**, *4*, 1643.

[103] M. W. Knight, H. Sobhani, P. Nordlander, N. J. Halas, *Science* **2011**, *332*, 702.

[104] W. Li, J. Valentine, *Nano Lett.* **2014**, *14*, 3510.

[105] Y. Zhan, K. Wu, C. Zhang, S. Wu, X. Li, *Opt. Lett.* **2015**, *40*, 4261.

[106] L. W. van Beveren, E. Panchenko, N. Anachi, L. Hyde, D. Smith, T. James, A. Roberts, J. McCallum in *2014 Conference on Optoelectronic and Microelectronic Materials & Devices*, IEEE, p. 144.

[107] H. Zhou, J. Mei, P. Gui, P. Tao, Z. Song, H. Wang, G.-J. Fang, *Mater. Sci. Semicond. Process.* **2015**, *38*, 67.

[108] M. Shasti, A. Mortezaali, R. Dariani, *J. Appl. Phys.* **2015**, *117*, 023101.

[109] J. Li, X. Wu, M. M. Shirolkar, M. Li, C. Xu, H. Wang, *RSC Adv.* **2017**, *7*, 18987.

[110] M. Albooyeh, C. R. Simovski, *Opt. Express* **2012**, *20*, 21888.

[111] J.-M. Manceau, S. Zanotto, T. Ongarello, L. Sorba, A. Tredicucci, G. Biasiol, R. Colombelli, *Appl. Phys. Lett.* **2014**, *105*, 081105.

[112] Y. Nishijima, A. Balcytis, S. Naganuma, G. Seniutinas, S. Juodkazis, *arXiv* **2018**, 1805.04726.

GRAPHICAL ABSTRACT